npj | climate and atmospheric science

Article

Published in partnership with CECCR at King Abdulaziz University

https://doi.org/10.1038/s41612-025-01120-x

Distinct bimodal size distribution in number concentration and light absorption of sub-500 nm brown carbon particles

Haobin Zhong[1,2,3], Wei Xu[2,3,4] ✉, Ru-Jin Huang[2] ✉, Chunshui Lin[2], Lu Yang[2], Yanan Zhan[2,5], Wei Huang[2], Jurgita Ovadnevaite[4], Darius Ceburnis[4] ✉ & Colin O'Dowd[4]

Brown carbon (BrC) aerosols impact climate and air quality through light absorption, but their size-resolved characteristics remain unclear. This study employs a novel positive matrix factorization (PMF) approach constrained by light absorption and marker fragment to derive the size distribution of the BrC number concentration and light absorption at high time and size resolutions. Our results show distinct bimodal patterns in the BrC number concentration for the sub-500 nm particles at Mace Head, the west coast of Ireland, with peaks at ~20 nm and 107 nm, attributable to new particle formation (nucleation mode) and subsequent growth processes to the accumulation mode, respectively. Light absorption also exhibited a bimodal distribution, with peaks at 137 nm and increasing values to 484 nm. This difference highlights that the larger particles (e.g. around 484 nm), though fewer in number (~3.6% of the total BrC particles), contribute significantly (~70%) to light absorption due to high mass concentration. The direct solar absorption of BrC relative to black carbon ranges from 1.7% to 4.8%, with a slight increase for particles larger than 100 nm, emphasizing the importance of larger particles in BrC radiative effects. These results offer insights into the size-resolved properties of sub-500 nm BrC, enhancing our understanding of BrC properties and potentially reducing uncertainties in aerosol-radiation interactions.

Brown carbon (BrC) aerosols, a subset of organic carbonaceous particulates exhibiting significant light absorption in the near-ultraviolet (300–400 nm) and visible light ranges[1–4], can exacerbate global warming[5–7]. Absorption by BrC also diminishes atmospheric photolysis rates for key radicals[8,9], influencing the secondary organic aerosol formation and air quality[10,11]. However, accurate quantification of BrC's radiative effects remains hindered by insufficient characterization, particularly regarding the size-dependent properties.

Size distribution is one of the most important but poorly understood properties of BrC, and plays a crucial role in regulating radiative budgets by determining the aerosol optical depth (AOD), which measures the light extinction in the atmospheric column due to both scattering and absorption[12,13]. Understanding the accurate size distribution across an extensive size range can help reduce uncertainties in estimating AOD[12]. Furthermore, the size distribution of BrC determines their contribution to cloud droplet activation. Incorporating BrC into cloud droplets may facilitate cloud evaporation via light absorption, adding an additional uncertainty to the estimation of aerosol-cloud interactions[14]. However, our understanding of the size distribution remains limited due to the challenges in accurately measuring the size-resolved light absorption of BrC. The size-dependent BrC light absorption properties can be obtained by using cascade impactors[15–17] or satellite remote sensing[18,19], but they suffer from poor temporal (mostly 24 h) or size resolutions (mostly maximum 13 or 22 segments for the cascade impactor or satellite remote sensing, respectively).

[1]School of Advanced Materials Engineering, Jiaxing Nanhu University, Jiaxing, China. [2]State Key Laboratory of Loess Science, Institute of Earth Environment, Chinese Academy of Sciences, Xi'an, China. [3]State Key Laboratory of Advanced Environmental Technology, Institute of Urban Environment, Chinese Academy of Sciences, Xiamen, China. [4]The Ryan Institute's Centre for Climate & Air Pollution Studies (C-CAPS), University of Galway, Galway, Republic of Ireland. [5]Institute of Global Environmental Change, School of Human Settlements and Civil Engineering, Xi'an Jiaotong University, Xi'an, China. ✉e-mail: wxu@iue.ac.cn; rujin.huang@ieecas.cn; darius.ceburnis@universityofgalway.ie

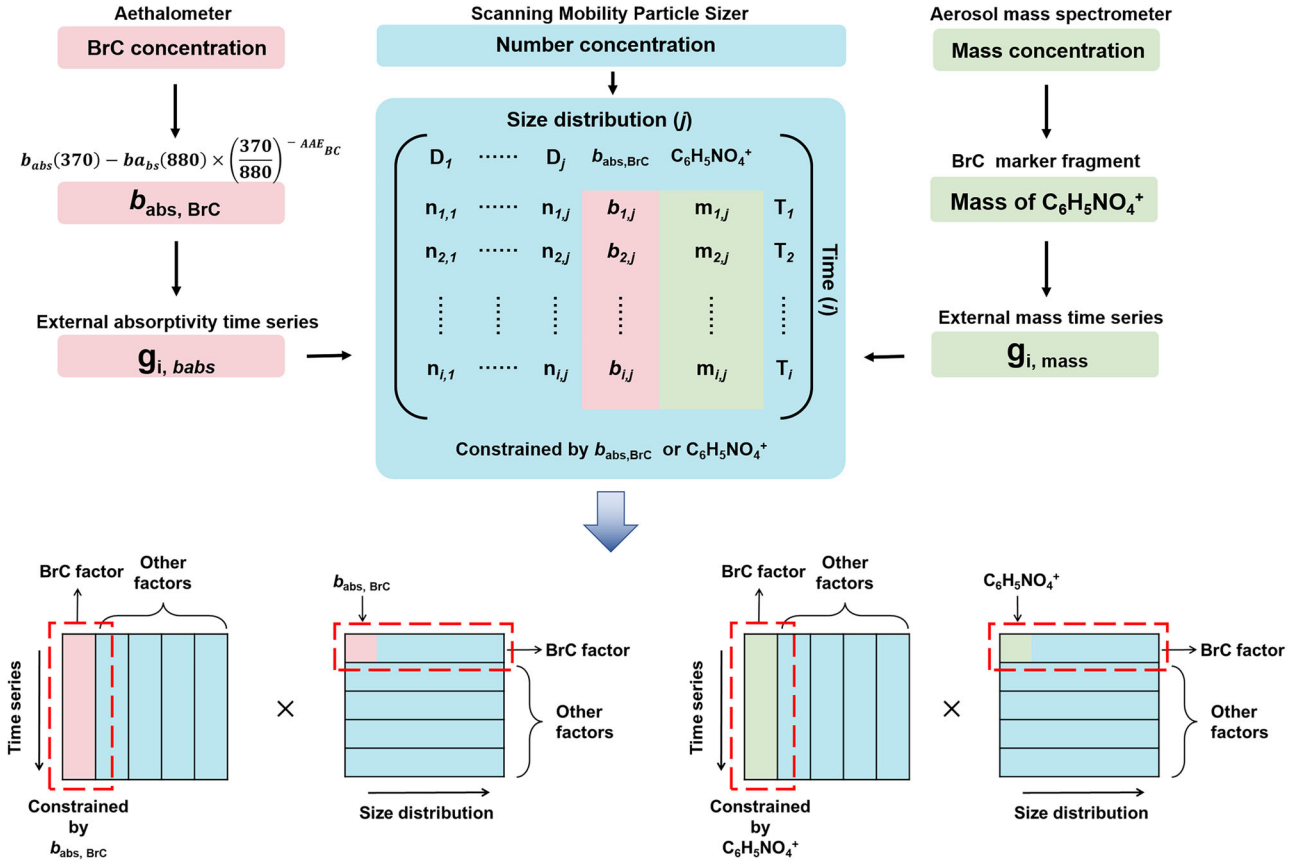

Fig. 1 | Schematic of the workflow. SMPS number concentration data (original matrix *X*) is decomposed by PMF into factor number size distribution (*F*) and time series (*G*) matrices. Constraints from $b_{abs,BrC}$ and $C_6H_5NO_4^+$ time series are applied to obtain the BrC number concentration size distribution factor.

Additionally, satellite remote sensing has high uncertainty (30%–50%) when the BrC fraction is less than 10%, leading to a less precise description of BrC[13,20].

Direct in-situ measurements of BrC light absorption as a function of size remain scarce due to limitations of current instrumentation in detecting BrC optical properties at high time and size resolutions. Some previous studies have provided valuable insights into the BrC size distributions. For example, Liu et al. [15] utilized cascade impactors to collect size-resolved aerosol samples for offline analysis, revealing that BrC chromophores predominantly exist in the accumulation mode with a mean aerodynamic diameter of 0.5 μm. Di Lorenzo et al. [16] collected size-resolved aerosols (10–18 μm) from aged wildfire plumes and found that BrC absorption was primarily in the fine-mode aerosols with molecular composition varying across different size fractions, showing distinct distribution patterns compared to the traditional biomass burning markers. Wu et al. [17]. analyzed size-resolved particles in Xi'an, China, demonstrating that water-extracted BrC predominantly occurred in the fine mode (<2.1 μm), accounting for 81% and 65% of total BrC absorption in winter and summer, respectively. These studies provide crucial understanding of the size-dependent properties of BrC, however, they relied on offline filter-based methods with limited size resolution, primarily yielding mass-based size distributions rather than number-based distributions. Therefore, new techniques are needed to obtain higher time- and size-resolved measurements of BrC number concentration and light absorption.

In this study, we introduce a novel positive matrix factorization (PMF) approach constrained by light absorption and BrC marker fragment to derive the size distribution of the BrC number concentration and light absorption at high time and size resolutions. Our analytical framework primarily relies on optical measurements, using BrC absorption data from an aethalometer for PMF&ME-2 constrained analysis to derive the number concentration size distribution of BrC particles. As complementary validation, we applied the same analytical framework to the time series of 4-nitrocatechol (4NC) fragments ($C_6H_5NO_4^+$) measured by aerosol mass spectrometry. Through the application of this methodology, we obtain the number size distribution and the light absorption size distribution of sub-500 nm brown carbon aerosols.

Results

Determination of BrC size factor

In this study, we employed the following workflow (as shown in Fig. 1) to decompose and identify the size distribution of BrC using PMF and Multilinear Engine version 2 (ME-2): Scanning mobility particle sizer (SMPS) data was averaged hourly to create the original matrix *X*, with rows (*j*) representing the time series and columns (*i*) representing the particle size distribution. PMF was applied using ME-2 with time series constraints from absorption coefficient of brown carbon ($b_{abs,BrC}$) measured by an aethalometer and $C_6H_5NO_4^+$ from synchronous aerosol mass spectrometer (AMS) observations. $b_{abs,BrC}$ represents changes in the BrC light absorption and was used to constrain particles related to BrC in the SMPS data. $C_6H_5NO_4^+$ has been confirmed in AMS studies as a characteristic fragment of nitrophenolic compounds such as 4-nitrocatechol (4NC)[21]. These compounds are recognized as important BrC components that contribute significantly to BrC light absorption in the near-UV and visible range[22–24]. We used this fragment to verify the reliability of the absorptivity constrained PMF results. PMF solutions with 2 to 8 factors were evaluated (Figs. S5 and S6) based on criteria explained in the methods section. Briefly, 6 factors were selected as the optimal solution based on the inflection point in Q/Q_{exp} ratio (close to ideal value of 1), clear factor separation, and strongest correlations with the external tracers. The factor exhibiting the highest explained variance of external data and strongest correlation to the $b_{abs,BrC}$

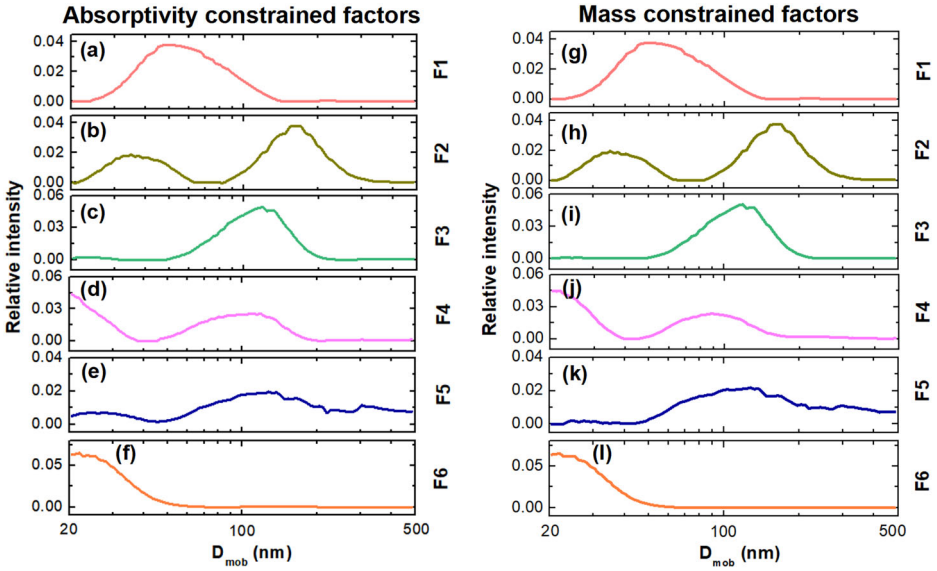

Fig. 2 | 6-factor PMF&ME2-resolved size distribution of BrC number concentration. Constraints applied: (**a**–**f**) aethalometer-derived $b_{abs,BrC}$ and (**g**–**l**) AMS-derived $C_6H_5NO_4^+$ signal.

or $C_6H_5NO_4^+$ time series was identified as the candidate BrC size distribution factor. Using this constrained PMF approach, we identified a robust BrC size distribution factor as detailed in the following sections.

Figure 2 shows the 6 factors resolved by the constrained PMF analysis and their number concentration size distribution characteristics. The left side (Fig. 2a–f) presents the $b_{abs,BrC}$ constrained results, while the right side shows the $C_6H_5NO_4^+$ constrained results. The patterns are similar between the two constraint methods.

Factors 1 and 2 exhibit size distributions similar to those reported for the traffic and mixed emissions in previous studies[25,26]. Further correlation analysis with chemical components revealed that Factor 1 correlates best with organic aerosol ($R = 0.64$; Fig. S7a, g). Factor 2 shows the highest correlation with nitrate ($R = 0.71$; Fig. S7b, h), while also maintaining a moderate correlation with organic aerosol ($R = 0.60$). Given that the light-absorbing components of organic aerosols were constrained to Factor 4 using the external time series, Factors 1 and 2 likely represent non-absorbing organic species and a mixture of non-absorbing organic species and nitrate (as evidenced by the improved correlation of Factor 2 with the sum of organic aerosol and nitrate, R increasing to 0.78, see Fig. S8), respectively. Factor 3 associates with sulfate ($R = 0.70$; Fig. S7c, i) and resembles the residential heating profiles[26,27]. Factor 4 represents the BrC factor and will be discussed in detail in the next section. Factor 5 represents sea spray ($R = 0.74$, Fig. S7d, k), with size distribution consistent with previous studies[28,29]. Factor 6 is the nucleation factor identified in previous studies[25,27,30]. The wind rose plot (Fig. S9f) shows that this factor reaches its highest concentration under low-speed (3–7 m/s) offshore winds (~135° direction), indicating the significant influence of land-sourced (mostly coastal seaweed beds during low tide) precursors on new particle formation at this coastal site. Under high-speed (>15 m/s) onshore wind conditions (180–210°), this factor also exhibits elevated concentrations, though slightly lower than those observed during offshore conditions.

The time series correlations (Fig. S7) and meteorological polar plots (Fig. S9) validate the factor determinations. Factor 5 derives from high offshore winds while Factors 1–4 originate onshore, confirming their gas- and particle-phase source differences. This supports the identification of Factor 4 as a robust BrC factor using the external constraints.

Number concentration size distribution of the BrC factor

Figure 3 shows the relative signal intensity and explained variance of factor 4 constrained by two external time series (Fig. 3a: $b_{abs,BrC}$ and Fig. 3e: $C_6H_5NO_4^+$), as well as their corresponding number concentration size distribution (Fig. 3b, f), scatter plots (Fig. 3c, g), and time series results (Fig. 3d, h). Factor 4 accounts for over 99% of explained variance in $b_{abs,BrC}$ and $C_6H_5NO_4^+$, confirming the resolved BrC factors. Additionally, the time series of the BrC factor is also highly correlated with the time series of $b_{abs,BrC}$ ($R = 0.93$), and $C_6H_5NO_4^+$ ($R = 0.99$), providing further evidence for the determination of this factor.

The number concentration size distribution of the BrC factor shows a bimodal pattern, with peaks in both nucleation and accumulation modes. A higher peak appears in the nucleation mode at 20 nm, accounting for 62.6% (absorptivity constrained results, similar in the mass constrained results) of the total BrC particle number (from 20 nm to 30 nm). This size distribution correlates well with the nucleation factor ($R = 0.62$), suggesting BrC formation during new particle formation processes[31]. Previous chemical composition studies at MHD provide valuable insights into potential BrC sources. Lawler et al. [32] conducted thermal desorption chemical ionization mass spectrometry (TD-CIMS) to characterize the molecular composition of particles within the 15–85 nm diameter range at MHD. Their analysis revealed the presence of $C_7H_7O_2^+$ ions, indicative of benzoic acid. This aromatic compound exhibits significant absorption cross-sections in the near-UV spectral region[33–35], suggesting its potential role as a primary chromophore contributing to the BrC optical signature observed in the nucleation and Aitken mode. Their investigation also identified the non-aromatic constituents, including nonanoic acid ($C_9H_{19}O_2^+$), formic acid ($CH_3O_2^+$), and hexanoic acid ($C_6H_{13}O_2^+$), which predominantly absorb below 220 nm. These species thus likely contribute negligibly to near-UV BrC absorption. The second peak centers at 107 nm with a relative intensity weaker than the first peak, accounting for 31.0% (absorptivity constrained results, similar in the mass constrained results) of the total BrC number (from 77 nm to 143 nm), corresponding to the accumulation mode distribution. This finding aligns with previous studies that have reported BrC in the accumulation mode, often associated with secondary organic aerosol formation and aging processes[15,36].

In addition, by comparing the results of the $b_{abs,BrC}$, and $C_6H_5NO_4^+$ constrained methods, we observed that the patterns of their number concentration size distribution are remarkably similar and their time series are also well correlated ($R = 0.63$, Fig. S10). The similarity between the BrC size distribution obtained from mass-constrained and light absorption-constrained PMF has led further confidence of robustness of this approach, especially considering that BrC and $C_6H_5NO_4^+$ were measured by different instruments based on different operational principles, indicating the validity of both constrained approaches.

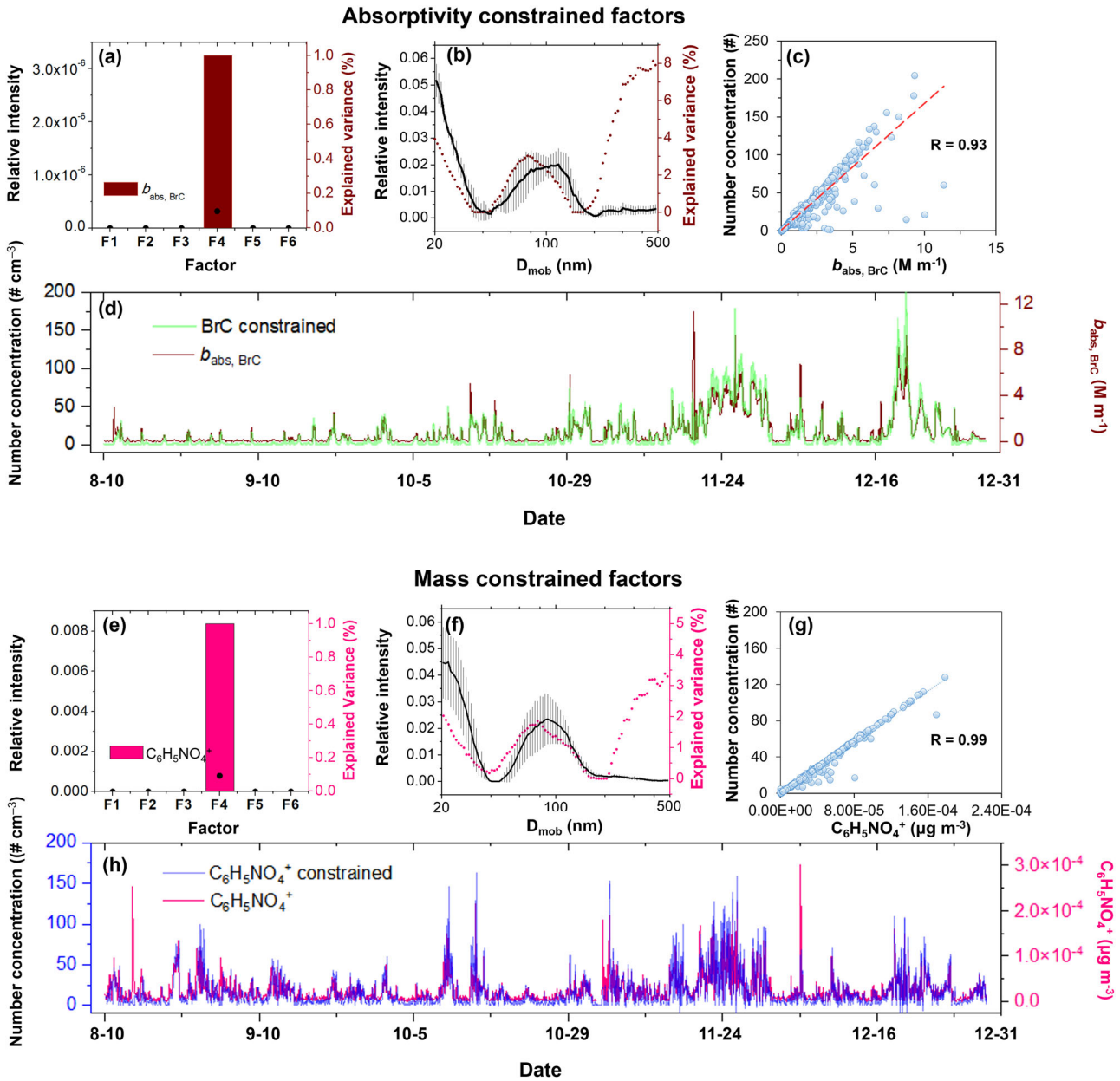

Fig. 3 | The BrC number concentration size distribution resolved by the PMF&ME-2 method. a, **e** are the results of the $b_{abs,BrC}$ and $C_6H_5NO_4^+$ dominated factors among the 6 factors. **b**, **f** Are the corresponding number concentration size distribution; the right axis represents the explained variance of specific component of the factor. **c**, **g** Aare the numerical concentration of the BrC factor and the correlation between $b_{abs,BrC}$ and $C_6H_5NO_4^+$, respectively, in addition to (**d**, **h**) their time series. Black vertical line in (**b**, **f**) represents the standard deviations of averaged iterative PMF&ME-2 result.

Size-resolved light absorption of the BrC factor

We further calculated the size-resolved $b_{abs,BrC}$ by converting the number concentration size distribution to mass size distribution and then multiplying it by the appropriate mass absorption efficiencies (MAE) of BrC at 370 nm. Recognizing that chemical composition likely varies across different particle sizes, we adopted a range-based approach to estimate the possible light absorption size distributions. Two boundary conditions were applied to estimate the possible light absorption size distributions: (1) assuming all particles have properties similar to primary emissions from biomass burning (MAE365 nm = 2.47 m^2 g^{-1}, representing an upper limit) and (2) assuming all particles have properties similar to clean marine environment (MAE365 nm = 0.98 m^2 g^{-1}, representing a lower limit)[37]. The results are shown in Fig. 4a, b, where the shaded areas represent the range between these upper and lower estimations, with the solid line indicating the average value.

The size-resolved $b_{abs,BrC}$ revealed a bimodal pattern of light absorption within the 20–484 nm range. Despite the presence of a large number of particles from 20 nm to 30 nm, their small mass results in negligible contribution to light absorption (0.006 ± 0.003 M m^{-1}), accounting for only 0.03% of the total BrC light absorption in the 20–484 nm range. One of the peaks occurs at 137 nm with $b_{abs,BrC}$ of 0.5 ± 0.2 M m^{-1} ($b_{abs,BrC}$ constrained) and 0.6 ± 0.3 M m^{-1} ($C_6H_5NO_4^+$ constrained), representing around 3.2–3.3% of the total BrC particle number (from 127 nm to 147 nm), demonstrating light absorption by BrC in the accumulation mode, accounting for approximately 36–40% of the total BrC light absorption. The other distribution shows increasing values of $b_{abs,BrC}$ starting from 211 nm (0.04 ± 0.02 M m^{-1} for $b_{abs,BrC}$ constrained and 0.05 ± 0.02 M m^{-1} for

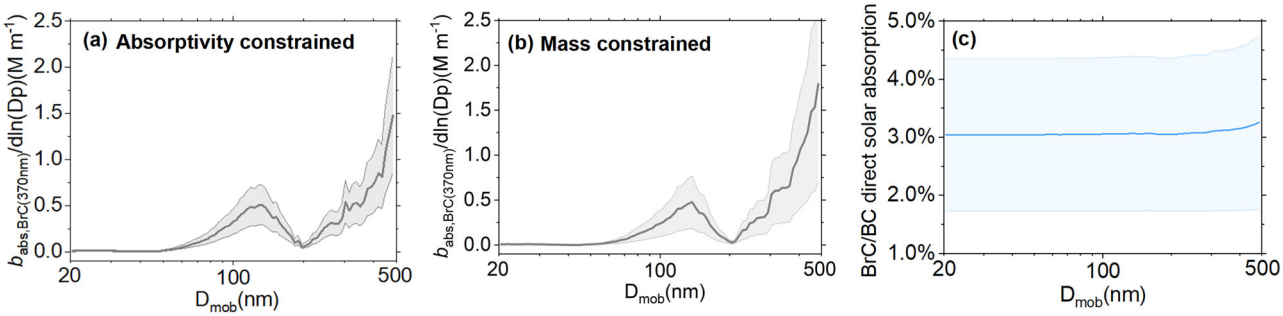

Fig. 4 | Size-resolved light absorption characteristics of BrC. a Absorption coefficient constrained by $b_{abs,BrC}$; (**b**) absorption coefficient constrained by $C_6H_5NO_4^+$; (**c**) direct solar absorption of BrC relative to BC (370–880 nm wavelength) in different size bins obtained by estimation. The shaded area represents the range of higher MAE results and lower MAE results.

$C_6H_5NO_4^+$ constrained) and continuing to rise rapidly until reaching its maximum value at the largest observable particle size of 484 nm (1.5 ± 0.6 M m^{-1} for $b_{abs,BrC}$ constrained and 1.7 ± 0.9 M m^{-1} for $C_6H_5NO_4^+$ constrained), representing around 3.2–3.6% of the total BrC particle number (from 211 nm to 484 nm), accounting for approximately 57–70% of the total BrC light absorption. It is worth noting that while the specific magnitude of light absorption may vary within the shaded areas depending on the actual chemical composition at different particle sizes, our range-based approach using minimum and maximum MAE values provides reasonable boundaries for the likely absorption characteristics across the entire size spectrum.

Also, we calculated the size-resolved direct solar absorption of BrC relative to BC across the wavelength range of 370–880 nm wavelength, as shown in Fig. 4(c). The change in the ratio of the direct solar absorption of BrC relative to BC is not pronounced in the 20–484 nm size range, but a slight increase can still be observed in the size range above 100 nm. In the results with higher MAE, the ratio of the direct solar absorption of BrC relative to BC increased from 4.4% to 4.8%. In the results with lower MAE, the ratio increased from 1.7% to 1.8%. The value of MAE has a relatively large impact on the ratio of the direct solar absorption of BrC relative to BC, but the overall ratio (1.7%–4.8%) has a small impact on solar absorption.

Discussion

This study demonstrates a novel PMF-constrained methodology to derive size-dependent properties of BrC. The approach provides new insights into the number concentration and light absorptivity across a wide sub-500 nm size range. It should be noted that the size distribution of BrC was assumed to be identical throughout the analysed period, which may not always be the case. BrC is a collective term for a subset of light-absorbing organic substances. As such, its particle size distribution is expected to vary depending on the sources, chemical compositions, and atmospheric processes.

The BrC size distribution obtained in this study should be considered as a weighted average related to the atmospheric transport pattern and sources around the MHD research station during the measurement period. We consider this assumption is reasonable for several reasons. First, using a long-term average (~4.5 months of data) inherently smooths out short-term fluctuations, capturing the dominant size distribution patterns that persist throughout the study period. Second, our analysis of meteorological patterns during this period indicates relatively consistent source regions affecting our measurement site, suggesting some stability in the aerosol population characteristics.

In reality, factors such as changes in biomass burning, secondary organic aerosol formation, and marine organic emissions could alter the size distribution of BrC over time. We acknowledge that in environments with highly variable or multiple distinct BrC sources, this assumption would require careful reconsideration. For instance, locations with strong seasonal variations in biomass burning activities, or urban areas with complex mixtures of traffic, industrial, and residential combustion sources, might exhibit more pronounced temporal variations in the BrC size distributions.

Additionally, aging processes such as photochemical bleaching or browning of organic aerosols can alter BrC optical properties over time. Our approach inherently incorporates these effects as they manifest in the measured optical signals but does not explicitly separate fresh from aged BrC. The derived size distributions therefore represent the ambient BrC population in various stages of atmospheric processing rather than source-specific or age-specific distributions.

Further research is needed to characterize how the BrC size distributions fluctuate under different source influences and atmospheric aging processes. Future studies could address this limitation by implementing time-dependent constraints or by conducting source-specific analyses when appropriate source markers are available.

Despite limitations in the consistent size distribution assumption, the insights gained can help reduce uncertainties in estimating BrC radiative impacts for climate models. The consistency between our optically constrained and chemically constrained results provides confidence in the overall approach, while acknowledging the simplifications necessary in this initial application. While further instrumentation could validate the absorption contributions across fine sizes, this practical methodology opens up new possibilities to investigate relationships between size and optical characteristics of BrC in diverse environments.

Methods

Measurement site and instrumentation

The measurements were carried out at the Mace Head Atmospheric research station (MHD), which is located on the West coast of Ireland (www.macehead.org). The station is situated at the interface of land and ocean, where winds from a direction between 180 and 300° reach it without passing over any inhabited area, while the rest of the surrounding rural area is sparsely populated[38]. The data was collected from 10th Aug. to 31st Dec. in 2018. A scanning mobility particles sizer (SMPS; DMA 3080 and CPC 3010, TSI Incorporated, Shoreview, MN, USA) was used to measure aerosol number concentration size distribution ranging from 20 to 484 nm. In recent years, many studies have combined PMF with SMPS data to distinguish the size distribution of particles from different sources[25–27,30,39–42]. The BC and BrC concentration were measured by an aethalometer (AE33, Magee Scientific, Berkeley, CA, USA)[43]. The concentration of the $C_6H_5NO_4^+$ (Fig. S1), a fragment indicative of brown carbon species such as 4-nitrocatechol (4NC)[21], was measured using a high-resolution time-of-flight aerosol mass spectrometer (HR-ToF-AMS, Aerodyne Research Inc., Billerica, MA, USA)[44]. Details and validation of the instrument can be found in our previous

reports[28,45]. An overview of the data is presented in Figs. S2–S4. To facilitate consistent analysis and comparison across different measurements, all data were averaged to a common 1-h resolution.

PMF&ME-2

In this study, PMF and ME-2 were used to obtain the size-resolved number concentration and light absorption coefficient of BrC. Essentially, PMF is a bilinear receptor model capable of separating the input data matrix into distinct factor matrices and their corresponding time series of concentrations (weight matrices)[46,47]. It is described as follows:

$$X = GF + E \tag{1}$$

where X represents the original matrix ($i \times j$) of the number concentration (i) and size distribution (j) of aerosols measured by SMPS. F and G denote the factor matrix ($p \times j$) of the size distribution (j) of aerosols under different factor numbers (p) and the weight matrix ($i \times p$) of the time series of number concentration (i) for each factor, respectively. E indicates the residual between the reconstructed matrix, calculated by multiplying F and G, and the original matrix X. To reduce the residual, the weighted sum of squared residuals was introduced in the calculations. By using least squares to iteratively minimize the sum of squared residuals in the receptor model computation, the PMF results are optimized. It is described as follows:

$$Q = \sum_{i=1}^{n} \sum_{j=1}^{m} \left(\frac{e_{ij}}{\sigma_{ij}} \right)^2 \tag{2}$$

where Q represents the sum of squared residuals after weighting, which is the ratio of the residual of the jth species (e_{ij}) in the ith hour in the matrix to its standard deviation (σ_{ij}). PMF has been widely applied in the studies of particle size distribution[25,27,39,40].

The multilinear engine method (ME-2) enables the incorporation of known external information to constrain PMF solutions[48]. In this study, we applied ME-2 constraining using the time series data of $b_{\mathrm{abs,BrC}}$, and $C_6H_5NO_4^+$ in conjunction with SMPS as an external weight matrix to conduct ME-2 calculations on the results as follows:

$$g_{i,solution} = g_i \pm a g_i \tag{3}$$

where $g_{i,solution}$ represents the weight matrix G obtained by solving the ME-2 algorithm. g_i denotes the introduced external weight matrix. This ensures the resolved the BrC factor corresponds to the external data, with the SMPS number concentration data entering each factor freely via unconstrained PMF.

In practice, we applied full constraints exclusively to the BrC factor by setting the a value to zero. This approach forced the BrC factor's time series (G matrix) to match the external data exactly, while allowing all other factors to remain completely unconstrained. To account for potential variability, we ran the ME-2 algorithm 100 times at the a value of zero. Each run yielded a number concentration size distribution (F matrix) for the tightly constrained the BrC factor. The final reported BrC size distribution is the average of these 100 runs, providing a robust solution despite the complete constraints. This tailored application of ME-2 builds on previous work utilizing constrained PMF for aerosol source apportionment[49,50]. All calculations related to ME-2 were performed on SourceFinder (6.3en, Datalystica, Ltd, Park InnovAARE, Villigen, Switzerland)[51] embedded in Igor Pro software (v6.37, WaveMetrics, Inc., Lake Oswego, OR, USA).

Error matrix

The uncertainty of size-resolved number concentration and external data was estimated by the method provided by the United States Environmental Protection Agency (USEPA) PMF 5.0 fundamentals and user guide as follows[52]:

$$Unc = \frac{5}{6} \times MDL \tag{4}$$

where MDL represents the method detection limit of the instrument.

Factor number determination

The PMF model quality is evaluated using the ratio Q/Q_{exp}. Q represents the sum of squared residuals weighted by uncertainty. Q_{exp} corresponds to the expected Q value based on degrees of freedom in the data[53,54].

Three criteria were sequentially followed to determine the optimal number of factors:

I. An inflection point in the plot of Q/Q_{exp} versus number of factors indicates the minimum number of factors needed to reproduce the data. Adding more factors beyond this point yields diminishing improvements in Q/Q_{exp}[55].
II. A Q/Q_{exp} value close to 1 suggests the model reproduces the true variability in the data based on the input error estimates[56].
III. The solution should minimize mixing or splitting of factors. Additionally, the BrC factor time series should correlate well with the external constraints.

The Q/Q_{exp} values (Figs. S5d and S6d) exhibit an inflection point at 6 factors in both constrained analyses. From 5 to 7 factors, Q/Q_{exp} ranges from 0.5–1.1 ($b_{abs,BrC}$ constrained) and 0.6–2.4 ($C_6H_5NO_4^+$ constrained), consistent with the ideal value of 1.

Since the Q/Q_{exp} ratio exhibited an inflection point at 6 factors, solutions with 5–7 factors were further evaluated. The particle size distribution of each factor and correlation of the BrC factor time series with external data were compared.

For 5 factors (Figs. S5a, S6a), no distinct BrC factor emerged. The sea spary distribution showed two peaks at 20–22 nm and 80–100 nm, indicating mixing with BrC. The external data correlation was lower ($R = 0.39$ for $b_{abs,BrC}$, $R = 0.37$ for $C_6H_5NO_4^+$) than for 6 or 7 factors.

With 7 factors (Figs. S5c, S6c), the results became unstable. The sea spray factor shape differed from literature reports[29]. For $b_{abs,BrC}$ constrained results, factors 1 and 2 showed similar distributions, potentially splitting a single factor. However, the BrC factor time series (factor 5) was highly correlated ($R = 0.99$ for $b_{abs,BrC}$, $R = 0.94$ for $C_6H_5NO_4^+$).

Considering Q/Q_{exp} values and factor characteristics, 6 factors were deemed optimal.

BrC light absorption coefficient

The light absorption Ångström Exponent (AAE) is used to characterize the wavelength dependence of aerosol optical absorption coefficient ($b_{\mathrm{abs}}(\lambda)$), and has been widely used in previous studies[57–60]. It describes as follows[12]:

$$b_{abs}(\lambda) \sim \lambda^{-\mathrm{AAE}} \tag{5}$$

At the Mace Head, impact of dust on the light absorption of aerosols is negligible, then $b_{\mathrm{abs}}(\lambda)$ can be divided into light absorption by BC ($b_{\mathrm{abs,BC}}(\lambda)$) and BrC ($b_{\mathrm{abs,BrC}}(\lambda)$)[59]. To determine the light absorption of BrC, it is necessary to obtain the light absorption of $b_{\mathrm{abs,\ BC}}$ at different wavelengths. Here, we assume that BC is the only absorbing substance at a wavelength of 880 nm[61], then $b_{\mathrm{abs,\ BC}}$ at other wavelengths can be calculated as follows[62]:

$$b_{abs,BC}(\lambda) = b_{abs}(880) \times \left(\frac{\lambda}{880} \right)^{-\mathrm{AAE_{BC}}} \tag{6}$$

where $\mathrm{AAE_{BC}}$ represents the BC spectral dependence, and a value of 1.1 was utilized based on prior research[59,63]. Then, $b_{\mathrm{abs,BrC}}$ can be calculated as

follows:

$$b_{abs,BrC}(\lambda) = b_{abs}(\lambda) - b_{abs}(880) \times \left(\frac{\lambda}{880}\right)^{-AAE_{BC}} \quad (7)$$

The maximum light absorption is observed at a wavelength of 370 nm in aethalometer. Consequently, in this study, light absorption of BrC at 370 nm ($b_{abs,BrC}(370)$) is used interchangeably with $b_{abs,BrC}$.

The direct solar absorption of BrC relative to BC was calculated using the method similar to Kirchstetter and Thatcher[64] and Kirillova et al. [65], and described in detail in Huang et al. [66]. It describes as follows:

$$f = \frac{\int I_0(\lambda)\left\{1 - e^{-b_{abs,BrC,\lambda} h_{ABL}}\right\} d\lambda}{\int I_0(\lambda)\left\{1 - e^{-b_{abs,BC,\lambda} h_{ABL}}\right\} d\lambda} \quad (8)$$

where $I_0(\lambda)$ is the clear sky Air Mass 1 Global Horizontal solar irradiance estimated by Levinson et al. [67] $b_{abs,BrC,\lambda}$ and $b_{abs,BC,\lambda}$ for BrC and BC denote the light absorption coefficient derived from the analysis described above. h_{ABL} represents to the boundary layer height (assuming 1000 m in this study).

Data availability

The hourly SMPS, aethalometer and AMS data in the paper may be requested from the corresponding authors upon reasonable request. The PMF analysis using ME-2 engine was conducted via the "SoFi" toolkit embedded in Igor Pro software can be found via https://datalystica.com.

Code availability

The hourly SMPS, aethalometer and AMS data in the paper may be requested from the corresponding authors upon reasonable request. The PMF analysis using ME-2 engine were conducted via the "SoFi" toolkit embedded in Igor Pro software can be found via https://datalystica.com.

Received: 8 January 2025; Accepted: 6 June 2025;
Published online: 23 June 2025

References

1. Bond, T. C. & Bergstrom, R. W. Light Absorption by carbonaceous particles: an investigative review. *Aerosol. Sci. Technol.* **40**, 27–67 (2006).
2. Ramanathan, V. et al. Atmospheric brown clouds: Hemispherical and regional variations in long-range transport, absorption, and radiative forcing. *J. Geophys. Res. Atmos*. **112**, D22S21 (2007).
3. Andreae, M. O. & Gelencsér, A. Black carbon or brown carbon? The nature of light-absorbing carbonaceous aerosols. *Atmos. Chem. Phys.* **6**, 3131–3148 (2006).
4. Feng, Y., Ramanathan, V. & Kotamarthi, V. R. Brown carbon: a significant atmospheric absorber of solar radiation? *Atmos. Chem. Phys.* **13**, 8607–8621 (2013).
5. Zhang, Y. et al. Top-of-atmosphere radiative forcing affected by brown carbon in the upper troposphere. *Nat. Geosci.* **10**, 486–489 (2017).
6. Brown, H. et al. Biomass burning aerosols in most climate models are too absorbing. *Nat. Commun.* **12**, 277 (2021).
7. Yue, S. et al. Brown carbon from biomass burning imposes strong circum-Arctic warming. *One Earth* **5**, 293–304 (2022).
8. Li, G., Bei, N., Tie, X. & Molina, L. T. Aerosol effects on the photochemistry in Mexico City during MCMA-2006/MILAGRO campaign. *Atmos. Chem. Phys.* **11**, 5169–5182 (2011).
9. Mok, J. et al. Impacts of brown carbon from biomass burning on surface UV and ozone photochemistry in the Amazon Basin. *Sci. Rep.* **6**, 36940 (2016).
10. Mohr, C. et al. Contribution of nitrated phenols to wood burning brown carbon light absorption in detling, United Kingdom during winter time. *Environ. Sci. Technol.* **47**, 6316–6324 (2013).
11. Moise, T., Flores, J. M. & Rudich, Y. Optical properties of secondary organic aerosols and their changes by chemical processes. *Chem. Rev.* **115**, 4400–4439 (2015).
12. Laskin, A., Laskin, J. & Nizkorodov, S. A. Chemistry of atmospheric brown carbon. *Chem. Rev.* **115**, 4335–4382 (2015).
13. Li, L. et al. Retrieval of aerosol components directly from satellite and ground-based measurements. *Atmos. Chem. Phys.* **19**, 13409–13443 (2019).
14. Hansen, J., Sato, M. & Ruedy, R. Radiative forcing and climate response. *J. Geophys. Res. Atmos.* **102**, 6831–6864 (1997).
15. Liu, J. et al. Size-resolved measurements of brown carbon in water and methanol extracts and estimates of their contribution to ambient fine-particle light absorption. *Atmos. Chem. Phys.* **13**, 12389–12404 (2013).
16. Di Lorenzo, R. A., Place, B. K., VandenBoer, T. C. & Young, C. J. Composition of size-resolved aged boreal fire aerosols: brown carbon, biomass burning tracers, and reduced nitrogen. *ACS Earth Space Chem* **2**, 278–285 (2018).
17. Wu, C. et al. The characteristics of atmospheric brown carbon in Xi'an, inland China: sources, size distributions and optical properties. *Atmos. Chem. Phys.* **20**, 2017–2030 (2020).
18. Schuster, G. L., Dubovik, O. & Arola, A. Remote sensing of soot carbon – Part 1: distinguishing different absorbing aerosol species. *Atmos. Chem. Phys.* **16**, 1565–1585 (2016).
19. Schuster, G. L., Dubovik, O., Arola, A., Eck, T. F. & Holben, B. N. Remote sensing of soot carbon – Part 2: understanding the absorption Ångström exponent. *Atmos. Chem. Phys.* **16**, 1587–1602 (2016).
20. Li, L. et al. Retrievals of fine mode light-absorbing carbonaceous aerosols from POLDER/PARASOL observations over East and South Asia. *Remote Sens. Environ.* **247**, 111913 (2020).
21. Bertrand, A. et al. Evolution of the chemical fingerprint of biomass burning organic aerosol during aging. *Atmos. Chem. Phys.* **18**, 7607–7624 (2018).
22. Harrison, M. A. et al. Nitrated phenols in the atmosphere: a review. *Atmos. Environ.* **39**, 231–248 (2005).
23. Yuan, W. et al. Measurement report: PM 2.5-bound nitrated aromatic compounds in Xi'an, Northwest China–seasonal variations and contributions to optical properties of brown carbon. *Atmos. Chem. Phys.* **21**, 3685–3697 (2021).
24. Laskin, A., West, C. P. & Hettiyadura, A. P. Molecular insights into the composition, sources, and aging of atmospheric brown carbon. *Chem. Soc. Rev.* **54**, 1583–1612 (2025).
25. Vu, T. V., Shi, Z. & Harrison, R. M. Estimation of hygroscopic growth properties of source-related sub-micrometre particle types in a mixed urban aerosol. *npj Clim. Atmos. Sci.* **4**, 21 (2021).
26. Ren, J. et al. Identifying the hygroscopic properties of fine aerosol particles from diverse sources in urban atmosphere and the applicability in prediction of cloud nuclei. *Atmos. Environ.* **298**, 119615 (2023).
27. Dai, Q. et al. Changes in source contributions to particle number concentrations after the COVID-19 outbreak: insights from a dispersion normalized PMF. *Sci. Total Environ.* **759**, 143548 (2021).
28. Ovadnevaite, J. et al. Submicron NE Atlantic marine aerosol chemical composition and abundance: Seasonal trends and air mass categorization. *J. Geophys. Res. Atmos.* **119**, 11,850–811,863 (2014).
29. Xu, W. et al. Sea spray as an obscured source for marine cloud nuclei. *Nat. Geosci.* **15**, 282–286 (2022).
30. Hopke, P. K., Feng, Y. & Dai, Q. Source apportionment of particle number concentrations: a global review. *Sci. Total Environ.* **819**, 153104 (2022).

31. Tian, X. et al. Monoethanolamine decay mediated by photolysis of nitrate in atmospheric particles: a brown carbon and organic phase formation pathway. *Environ. Sci. Atmos.* **3**, 1541–1551 (2023).
32. Lawler, M. et al. Composition of 15–85 nm particles in marine air. *Atmos. Chem. Phys.* **14**, 11557–11569 (2014).
33. Lund Myhre, C. & Nielsen, C. J. Optical properties in the UV and visible spectral region of organic acids relevant to tropospheric aerosols. *Atmos. Chem. Phys.* **4**, 1759–1769 (2004).
34. Jacobson, M. Z. Isolating nitrated and aromatic aerosols and nitrated aromatic gases as sources of ultraviolet light absorption. *J. Geophys. Res. Atmos* **104**, 3527–3542 (1999).
35. Lin, P. et al. Molecular characterization of brown carbon in biomass burning aerosol particles. *Environ. Sci. Technol.* **50**, 11815–11824 (2016).
36. Li, Y. et al. Unexpected oligomerization of small α-dicarbonyls for secondary organic aerosol and brown carbon formation. *Environ. Sci. Technol.* **55**, 4430–4439 (2021).
37. Geng, X. et al. Source apportionment of water-soluble brown carbon in aerosols over the northern South China Sea: Influence from land outflow, SOA formation and marine emission. *Atmos. Environ.* **229**, 117484 (2020).
38. O'Connor, T. C., Jennings, S. G. & O'Dowd, C. D. Highlights of fifty years of atmospheric aerosol research at Mace Head. *Atmos. Res.* **90**, 338–355 (2008).
39. Harrison, R. M., Beddows, D. C. S. & Dall'Osto, M. PMF analysis of wide-range particle size spectra collected on a major highway. *Environ. Sci. Technol.* **45**, 5522–5528 (2011).
40. Dall'Osto, M. et al. Urban aerosol size distributions over the Mediterranean city of Barcelona, NE Spain. *Atmos. Chem. Phys.* **12**, 10693–10707 (2012).
41. Srivastava, D. et al. Insight into PM2.5 sources by applying positive matrix factorization (PMF) at urban and rural sites of Beijing. *Atmos. Chem. Phys.* **21**, 14703–14724 (2021).
42. Rowell, A. et al. Insights into the sources of ultrafine particle numbers at six European urban sites obtained by investigating COVID-19 lockdowns. *Atmos. Chem. Phys.* **24**, 9515–9531 (2024).
43. Drinovec, L. et al. The "dual-spot" Aethalometer: an improved measurement of aerosol black carbon with real-time loading compensation. *Atmos. Meas. Tech.* **8**, 1965–1979 (2015).
44. DeCarlo, P. F. et al. Field-deployable, high-resolution, time-of-flight aerosol mass spectrometer. *Anal. Chem.* **78**, 8281–8289 (2006).
45. Ovadnevaite, J. et al. On the effect of wind speed on submicron sea salt mass concentrations and source fluxes. *J. Geophys. Res. Atmos*. **117**, D16201 (2012).
46. Paatero, P. & Tapper, U. Positive matrix factorization: a non-negative factor model with optimal utilization of error estimates of data values. *Environmetrics* **5**, 111–126 (1994).
47. Paatero, P. Least squares formulation of robust non-negative factor analysis. *Chemom. Intell. Lab. Syst.* **37**, 23–35 (1997).
48. Paatero, P. The multilinear engine—a table-driven, least squares program for solving multilinear problems, including the n-Way parallel factor analysis model. *J. Comput. Graph. Stat.* **8**, 854–888 (1999).
49. Beddows, D. C. S. & Harrison, R. M. Receptor modelling of both particle composition and size distribution from a background site in London, UK – a two-step approach. *Atmos. Chem. Phys.* **19**, 4863–4876 (2019).
50. Lin, C. et al. Comprehensive source apportionment of submicron aerosol in shijiazhuang, china: secondary aerosol formation and holiday effects. *ACS Earth Space Chem.* **4**, 947–957 (2020).
51. Canonaco, F., Crippa, M., Slowik, J. G., Baltensperger, U. & Prévôt, A. S. H. SoFi, an IGOR-based interface for the efficient use of the generalized multilinear engine (ME-2) for the source apportionment: ME-2 application to aerosol mass spectrometer data. *Atmos. Meas. Tech.* **6**, 3649–3661 (2013).
52. Polissar, A. V., Hopke, P. K., Paatero, P., Malm, W. C. & Sisler, J. F. Atmospheric aerosol over Alaska: 2. Elemental composition and sources. *J. Geophys. Res. Atmos.* **103**, 19045–19057 (1998).
53. Paatero, P. & Tapper, U. Analysis of different modes of factor analysis as least squares fit problems. *Chemom. Intell. Lab. Syst.* **18**, 183–194 (1993).
54. Paatero, P., Hopke, P. K., Song, X.-H. & Ramadan, Z. Understanding and controlling rotations in factor analytic models. *Chemom. Intell. Lab. Syst.* **60**, 253–264 (2002).
55. Seinfeld, J. H. & Pandis, S. N. *Atmospheric chemistry and physics: from air pollution to climate change* (John Wiley & Sons, 2016).
56. Isokääntä, S. et al. Comparison of dimension reduction techniques in the analysis of mass spectrometry data. *Atmos. Meas. Tech.* **13**, 2995–3022 (2020).
57. Qin, Y. M. et al. Chemical characteristics of brown carbon in atmospheric particles at a suburban site near Guangzhou, China. *Atmos. Chem. Phys.* **18**, 16409–16418 (2018).
58. Li, S. et al. Filter-based measurement of light absorption by brown carbon in PM2. 5 in a megacity in South China. *Sci. Total Environ.* **633**, 1360–1369 (2018).
59. Wang, Q. et al. Wintertime optical properties of primary and secondary brown carbon at a regional site in the North China Plain. *Environ. Sci. Technol.* **53**, 12389–12397 (2019).
60. Liakakou, E. et al. Long-term brown carbon spectral characteristics in a Mediterranean city (Athens). *Sci. Total Environ.* **708**, 135019 (2020).
61. Kirchstetter, T. W., Novakov, T. & Hobbs, P. V. Evidence that the spectral dependence of light absorption by aerosols is affected by organic carbon. *J. Geophys. Res. Atmos*. **109**, D21208 (2004).
62. Shamjad, P. et al. Contribution of brown carbon to direct radiative forcing over the Indo-Gangetic Plain. *Environ. Sci. Technol.* **49**, 10474–10481 (2015).
63. Lack, D. & Langridge, J. On the attribution of black and brown carbon light absorption using the Ångström exponent. *Atmos. Chem. Phys.* **13**, 10535–10543 (2013).
64. Kirchstetter, T. & Thatcher, T. Contribution of organic carbon to wood smoke particulate matter absorption of solar radiation. *Atmos. Chem. Phys.* **12**, 6067–6072 (2012).
65. Kirillova, E. N. et al. Water-soluble organic carbon aerosols during a full New Delhi winter: isotope-based source apportionment and optical properties. *J. Geophys. Res. Atmos.* **119**, 3476–3485 (2014).
66. Huang, R.-J. et al. Brown carbon aerosol in Urban Xi'an, Northwest China: the composition and light absorption properties. *Environ. Sci. Technol.* **52**, 6825–6833 (2018).
67. Levinson, R., Akbari, H. & Berdahl, P. Measuring solar reflectance—Part I: defining a metric that accurately predicts solar heat gain. *Sol. Energy* **84**, 1717–1744 (2010).

Acknowledgements

This work was supported by the National Natural Science Foundation of China (NSFC) under Grant No. 42525301, No. 42430708, No. 42277092, No. 42107126, the Key Research Program of Frontier Sciences from the Chinese Academy of Sciences (ZDBS-LY-DQC001), the New Cornerstone Science Foundation through the XPLORER PRIZE, the National Key Research and Development Program of China (grant No. 2023YFC3705503), the Hundred-Talent Program of the Chinese Academy of Sciences, the EPA-Ireland and Department of the Environment, Climate and Communications, SFI FFP award (22/FFP-A/10611), the Personal Startup Funding of Jiaxing Nanhu University (grant No. QD61220045). We would like to acknowledge Yao Qu of the Institute of Earth Environment, Chinese Academy of Sciences for the useful discussion on the relative direct solar absorption calculation.

Author contributions

H.Z., W.X., R.-J.H., and D.C. designed the study. Data analysis was done by H.Z. and W.X. H.Z. and W.X. wrote the initial draft, and all authors commented on and discussed the manuscript.

Competing interests

The authors declare no competing interests.

Additional information

Supplementary information The online version contains supplementary material available at https://doi.org/10.1038/s41612-025-01120-x.

Correspondence and requests for materials should be addressed to Wei Xu, Ru-Jin Huang or Darius Ceburnis.